Calibration techniques for single-sensor ultrasound imaging with a coding mask

Pim van der Meulen*, Pieter Kruizinga†‡, Johannes G. Bosch‡, Geert Leus*

*Delft University of Technology, Circuits and Systems, Delft, Netherlands
†Erasmus Medical Center, Department of Neuroscience, Rotterdam, Netherlands
‡Erasmus Medical Center, Biomedical Engineering, Rotterdam, Netherlands

***Abstract*—We consider a model-based ultrasound imaging scenario using a single transducer with a coding mask, and assume that the pulse-echo model is erroneously estimated, resulting in decreased imaging performance. Although the pulse-echo Green's function to each pixel has to be measured to obtain a good model, typically only forward-field measurements are obtained for better SNR, from which the pulse-echo Green's functions are estimated. However, if the transducer's receive transfer function is different from the transmit transfer function, the forward-field measurements do not incorporate the receive transfer function, resulting in an incorrect pulse-echo model. We propose two calibration techniques that start with this erroneous model, and update it using pulse-echo measurements. In the first technique we assume the calibration phantom is known a priori, whereas in the second technique we use multiple random calibration phantoms of which only the second-order statistics are assumed to be known beforehand. Both methods are able to significantly improve the pulse-echo model, strongly improving imaging performance. Our simulation results show that the first technique works best, since there is no uncertainty about the calibration image, whereas the blind calibration technique requires no exact knowledge of the calibration phantom, making it robust to positioning or manufacturing errors.**

I. Introduction

Model-based image reconstruction from pulse-echo measurements requires a well-calibrated pulse-echo model relating the ultrasound image to the pulse-echo measurements. We consider model calibration for ultrasound imaging with a device consisting of only a single sensor with a coding mask. In particular, we assume a linear measurement model, where the Green's functions are calibrated correctly for each pixel, but the electro-mechanical transducer transfer function is incorrectly estimated. Using only pulse-echo measurements, we then want to update the model, in case the transmit and receive transfer function of the transducer are not identical.

Model-based ultrasound imaging takes into account the known physics of the ultrasound imaging problem. The waveform of the transmitted pulse, as well as the Green's functions and transducer transfer functions can be exploited when reconstructing the ultrasound image from the measured pulse-echo signals. Model-based imaging approaches have been applied to linear arrays [1]–[8], where typically the first-order Born approximation is used to express pulse-echo measurements as a linear function of the unknown image, although this relation may be more complex for actual experimental measurements.

Exploiting all possible information in measurements is not only useful for better imaging algorithms, but can also help to enable image reconstruction in scenarios where measurements are sampled below Nyquist rate (either spatially or temporally) in order to reduce the amount of measurement data. Such undersampling, or compression, is becoming increasingly more important when there is an unmanageable amount of measurement data (e.g. for large 2D arrays), or when we can only use a limited amount of sensors (e.g. due to space limitations in imaging probes for minimally invasive surgery). This demand for compressing measurement data has led to a number of studies ([9]–[15], among others) in the field of medical ultrasound imaging using compressive sensing (CS) techniques [16]–[18], some of them relying on an accurate model of the pulse-echo field for reconstruction.

Recently, we proposed a measurement setup using only a single ultrasound sensor with a coding mask [19], [20]. Due to the large aperture size of the single sensor with respect to the wavelength, spatial measurements are effectively encoded into the temporal dimension of the output signals by the coding mask placed in front of the transducer. Because of the lack of spatial measurements, this imaging technique is more dependent on accurate modeling of the temporal pulse-echo signals.

To acquire an accurate model of the pulse-echo signal of each pixel, one would have to place a small reflector in each pixel position, and measure each pixel separately. This would result in very low SNR, so instead we measure the transmit field of the masked transducer in a plane, for each pixel in the plane, after which we can virtually propagate this field to any point in space (see [19] for more details). Subsequently, the pulse-echo signal for each potential reflector can be estimated from this measurement of the forward field.

Although we can assume that each Green's function between a pixel and the transducer is reciprocal, and thus can estimate the pulse-echo Green's function from the forward Green's function, we may not assume that the electro-mechanical transfer function is the same for transmit and receive (depending on the transducer transmit and receive

This work is part of the ASPIRE project (project 14926 within the STW OTP programme), and the PUMA project (project 13154 within the STW OTP programme), which are financed by the Netherlands Organisation for Scientific Research (NWO).

electrical matching networks and impedances [21], [22]). As a result, we can correctly estimate the pulse-echo Green's functions from forward-only measurements, but not the transducer transfer function. Hence, we will consider several calibration techniques to correct for this model mismatch. We assume that an incorrect measurement model is obtained from measuring the forward field, and subsequently try to update this model using conventional pulse-echo measurements.

II. Signal model

Using the first-order Born approximation (no multiple scattering between reflectors), we assume that any pulse-echo measurement is a linear function of the ultrasound image. More specifically, we use the following measurement equation:

$$\mathbf{y} = \mathbf{A}\mathbf{x} + \mathbf{n}, \tag{1}$$

where $\mathbf{y} \in \mathbb{C}^M$ is the complex vector of frequency samples of the sampled pulse-echo signal, and $\mathbf{A} \in \mathbb{C}^{M\times N}$ is a complex matrix containing Green's functions between each pixel and the transducer, thereby relating each measurement to the discretized image $\mathbf{x} \in \mathbb{R}^N$. The vector $\mathbf{n} \in \mathbb{C}^M \sim \mathcal{CN}(\mathbf{0}, \sigma_n^2\mathbf{I})$ contains i.i.d. white complex Gaussian measurement noise, N is the number of pixels, and M is the number of measurement samples. Since $\mathbf{A}$ is typically an ill-posed matrix, we will assume that an ultrasound image is obtained using a regularized estimate of $\mathbf{x}$ from $\mathbf{y}$:

$$\hat{\mathbf{x}} = \arg\min_{\mathbf{x}} \|\mathbf{y} - \mathbf{A}\mathbf{x}\|_2^2 + \lambda\|\mathbf{x}\|_2^2, \tag{2}$$

where λ is a regularization parameter, which we will set to σ_n^2 for all imaging experiments. This corresponds to using the Wiener estimate of $\mathbf{x}$ assuming that the covariance matrix of $\mathbf{x}$ is the identity matrix. Although the identity matrix does not accurately describe the structure in the true ultrasound image, it will prevent large values in the solution $\hat{\mathbf{x}}$ without imposing an explicit structure on $\hat{\mathbf{x}}$, instead relying on the data fidelity term $\|\mathbf{y}-\mathbf{A}\mathbf{x}\|_2^2$ to obtain an estimate of the ultrasound image.

Next, we assume that an estimate of $\mathbf{A}$, denoted by $\hat{\mathbf{A}}$, is obtained from a calibration procedure using experimental data of the actual measurement setup. A straightforward approach would be to put a small (approximately the same size as the wavelength) scatterer in each pixel position, and measure its pulse-echo response. The drawback of such an approach is the relatively low SNR, since the small reflector would only reflect a small fraction of the incident wavefield. Instead, we try to infer the pulse-echo signals of all pixels by only measuring the forward field using a hydrophone (a small calibrated microphone membrane at the tip of a needle), then obtain a rough estimate of $\mathbf{A}$, and finally update $\mathbf{A}$ using pulse-echo measurements from arbitrary objects with good SNR.

For a linear propagation and scattering model, the pressure signal $u_m(t)$ measured at pixel m can be described as a convolution of the excitation pulse $e(t)$, the transmit impulse response $g_{tx}(t)$, and the Green's function $h(t, \mathbf{p}_m)$ [23]–[25]:

$$u_m(t) = e(t) * g_{tx}(t) * h(t, \mathbf{p}_m), \tag{3}$$

where $\mathbf{p}_m \in \mathbb{R}^3$ is the position of pixel m, and * denotes the temporal convolution operator. Using the reciprocity principle, we then estimate the pulse-echo response $a_m(t)$ of pixel m as the auto-convolution $\hat{a}_m(t) = u_m(t) * u_m(t)$:

$$\begin{aligned}\hat{a}_m(t) &= u_m(t) * u_m(t) \\ &= e(t) * g_{tx}(t) * h(t, \mathbf{p}_m) * h(t, \mathbf{p}_m) * g_{tx}(t) * e(t),\end{aligned} \tag{4}$$

whereas the true pulse-echo signal is:

$$a_m(t) = e(t) * g_{tx}(t) * h(t, \mathbf{p}_m) * h(t, \mathbf{p}_m) * g_{rx}(t). \tag{5}$$

Equations (4) and (5) show that the error in the estimated pulse-echo signal is caused by the term $e(t) * e(t)$, and by the fact that generally $g_{tx}(t) \neq g_{rx}(t)$. The first error can be resolved by making sure that the pulse length of $e(t)$ is approximately one sample in time, such that $e(t) * e(t) \approx \delta(t) * \delta(t) = \delta(t) = e(t)$. Resolving the second error will be the focus of the remainder of this paper.

We will assume that there exists a signal $c(t)$ that corrects for this mismatch such that $a_m(t) = c(t) * \hat{a}_m(t)$. Besides the mismatch between (4) and (5), $c(t)$ can also correct for any other un-modeled effects, or remove model errors introduced by e.g. the hydrophone impulse response used for measuring the forward field. Note that $c(t)$ can only be used to update the temporal frequencies in $\hat{\mathbf{A}}$ that are within the bandwidth of $\hat{a}_m(t)$. Since the impulse response mismatch is common for all pixels, we can rewrite (1) as:

$$\mathbf{y} = \mathrm{diag}(\mathbf{c})\hat{\mathbf{A}}\mathbf{x} + \mathbf{n}, \tag{6}$$

where $\mathbf{c} \in \mathbb{C}^M$ is the DFT of $c(t)$, and $\hat{\mathbf{A}}$ is an estimate of the true matrix $\mathbf{A}$, obtained using the auto-convolution method described above. The calibration problem consists of estimating $\mathbf{c}$ from the measurement $\mathbf{y}$, having some prior knowledge on $\mathbf{x}$. In the remainder of this paper we study two cases: one where $\mathbf{x}$ is fully known, and one where $\mathbf{x}$ is seen as a random variable with known covariance matrix.

III. Calibration with a known phantom

We first consider the case of a single transducer with a coding mask, obtaining additional measurements by rotating the mask in slow-time. We further assume that a static calibration phantom $\mathbf{x}_c$ is known. Denoting the measurement equation for the pulse-echo measurement with the mask rotated at angle ϕ by $\mathbf{A}_\phi$, the total measurement equation for Φ measurements is:

$$\begin{bmatrix}\mathbf{y}_1\\ \mathbf{y}_2\\ \vdots\\ \mathbf{y}_\Phi\end{bmatrix} = \begin{bmatrix}\mathrm{diag}(\mathbf{c})\hat{\mathbf{A}}_1\\ \mathrm{diag}(\mathbf{c})\hat{\mathbf{A}}_2\\ \vdots\\ \mathrm{diag}(\mathbf{c})\hat{\mathbf{A}}_\Phi\end{bmatrix}\mathbf{x}_c + \mathbf{n}. \tag{7}$$

Since we use the same measurement setup across all measurements ϕ, the signal $\mathbf{c}$ should not change, and it appears multiple times in (7). Consequently, (7) can be explicitly

rewritten in terms of only $\mathbf{c}$:

$$\begin{bmatrix}\mathbf{y}_1\\ \mathbf{y}_2\\ \vdots\\ \mathbf{y}_\Phi\end{bmatrix} = \begin{bmatrix}\text{diag}(\hat{\mathbf{A}}_1\mathbf{x}_c)\\ \text{diag}(\hat{\mathbf{A}}_2\mathbf{x}_c)\\ \vdots\\ \text{diag}(\hat{\mathbf{A}}_\Phi\mathbf{x}_c)\end{bmatrix}\mathbf{c} + \mathbf{n}, \tag{8}$$

From (8), it is straightforward to estimate $\mathbf{c}$ by minimizing

$$\hat{\mathbf{c}} = \arg\min_{\mathbf{c}} \|\tilde{\mathbf{y}} - \tilde{\mathbf{A}}\mathbf{c}\|_2^2 + \lambda_{c1}\|\mathbf{c}\|_2^2, \tag{9}$$

where $\tilde{\mathbf{A}} = [\text{diag}(\hat{\mathbf{A}}_1\mathbf{x}_c)\ \text{diag}(\hat{\mathbf{A}}_2\mathbf{x}_c)\ \ldots\ \text{diag}(\hat{\mathbf{A}}_\Phi\mathbf{x}_c)]^\mathsf{T}$, and $\tilde{\mathbf{y}} = [\mathbf{y}_1^\mathsf{T}\ \mathbf{y}_2^\mathsf{T}\ \ldots\ \mathbf{y}_\Phi^\mathsf{T}]^\mathsf{T}$. The term $\|\mathbf{c}\|_2^2$ is used to regularize the problem due to the presence of rows in $\tilde{\mathbf{A}}$ with entries close to zero, and λ_{c1} is the regularization parameter, which we will set proportional to σ_n^2.

IV. Blind calibration

As an alternative calibration method, we can consider estimating $\mathbf{c}$ if $\mathbf{x}_c$ itself is not known, but assuming that we have some prior statistical information about $\mathbf{x}_c$. Specifically, we will assume that $\mathbf{x}_c$ can be regarded as a random signal with a known covariance matrix $\mathbf{C}_x$. This is advantageous compared to non-blind calibration, since $\mathbf{x}_c$ does not have to be known exactly. For example, the calibration phantom may not be positioned correctly, causing $\mathbf{y}$ to be a measurement corresponding to a rotated and/or translated version of $\mathbf{x}_c$. Moreover, there could be manufacturing errors, so that the true $\mathbf{x}_c$ is not known, but only an approximation of it. Instead of taking these errors into account explicitly, we will not directly assume anything about the shape of the phantom, but view $\mathbf{x}_c$ as a realization of a random variable with covariance matrix $\mathbf{C}_x$.

For example, a water tank with a large amount of moving air or micro bubbles ([26], [27]) could be utilized as calibration phantom. Between each pulse-echo measurement the bubbles will have moved and a new 'realization' of the random process is observed. One could also create a solid phantom with many small reflectors inside, generated according to a random process with spatial covariance $\mathbf{C}_x$. By rotating or translating the transducer across the phantom over a sufficient distance, multiple independent realizations are acquired.

More formally, suppose we collect K pulse-echo measurements $\{\mathbf{y}_k\}_{k=1}^K$, where each $\mathbf{y}_k$ is measured from a different realization of $\mathbf{x}_c$ based on the same true model $\mathbf{A}$, and corresponding estimated model $\hat{\mathbf{A}}$. Furthermore, assuming that $\mathbf{x}_c$ and $\mathbf{n}$ are uncorrelated variables, we have

$$\mathbb{E}\{\mathbf{y}\mathbf{y}^\mathsf{H}\} = \mathbb{E}\{(\mathbf{A}\mathbf{x}_c + \mathbf{n})^\mathsf{H}(\mathbf{A}\mathbf{x}_c + \mathbf{n})\} \tag{10}$$

$$= \mathbb{E}\{\text{diag}(\mathbf{c})\hat{\mathbf{A}}\mathbf{x}_c\mathbf{x}_c^\mathsf{H}\hat{\mathbf{A}}^\mathsf{H}\text{diag}(\mathbf{c})^\mathsf{H}\} + \mathbb{E}\{\mathbf{n}\mathbf{n}^\mathsf{H}\} \tag{11}$$

$$= \text{diag}(\mathbf{c})\hat{\mathbf{A}}\mathbf{C}_x\hat{\mathbf{A}}^\mathsf{H}\text{diag}(\mathbf{c})^\mathsf{H} + \sigma_n^2\mathbf{I}. \tag{12}$$

After obtaining an estimate of $\mathbb{E}\{\mathbf{y}\mathbf{y}^\mathsf{H}\}$ using:

$$\hat{\mathbf{C}}_y = \frac{1}{K}\sum_{k=1}^{K}\mathbf{y}\mathbf{y}^\mathsf{H}, \tag{13}$$

we want to estimate $\mathbf{c}$ from $\hat{\mathbf{C}}_y$. This is a problem that can be solved using 'covariance matching' techniques [28], and has been applied in the context of model calibration for radio astronomy arrays, where the problem structure is very similar to ours [29]. Instead of minimizing the maximum likelihood cost function for $\mathbf{c}$, which is non-convex, the covariance matching approach instead minimizes

$$\|\hat{\mathbf{C}}_y - \text{diag}(\mathbf{c})\hat{\mathbf{A}}\mathbf{C}_x\hat{\mathbf{A}}^\mathsf{H}\text{diag}(\mathbf{c})^\mathsf{H} - \sigma_n^2\mathbf{I}\|_F^2 \tag{14}$$

with respect to $\mathbf{c}$.

In this paper, we will use the recently proposed method in [30] to minimize (14). It is based on the observation that

$$\text{diag}(\mathbf{c})\hat{\mathbf{A}}\mathbf{C}_x\hat{\mathbf{A}}^\mathsf{H}\text{diag}(\mathbf{c})^\mathsf{H} = (\hat{\mathbf{A}}\mathbf{C}_x\hat{\mathbf{A}}^\mathsf{H}) \circ (\mathbf{c}\mathbf{c}^\mathsf{H}) \tag{15}$$

$$= (\hat{\mathbf{A}}\mathbf{C}_x\hat{\mathbf{A}}^\mathsf{H}) \circ \mathbf{C}_c \tag{16}$$

if $\text{rank}(\mathbf{C}_c) = 1$. By relaxing this non-convex rank constraint to a positive semi-definite constraint, we obtain a convex relaxation to estimate $\mathbf{c}\mathbf{c}^\mathsf{H}$:

$$\hat{\mathbf{C}}_c = \arg\min_{\mathbf{C}_c} \|\hat{\mathbf{C}}_y - (\hat{\mathbf{A}}\mathbf{C}_x\hat{\mathbf{A}}^\mathsf{H}) \circ \mathbf{C}_c - \sigma_n^2\mathbf{I}\|_F^2, \quad \text{s.t. } \mathbf{C}_c \succeq \mathbf{0}, \tag{17}$$

where $\mathbf{C}_c \succeq \mathbf{0}$ means $\mathbf{C}_c$ is a positive semi-definite matrix, and $\circ$ is the element-wise matrix product. If $\text{rank}(\hat{\mathbf{C}}_c) = 1$, we have obtained the minimizer of (14). If not, we obtain the closest rank-1 approximation to $\hat{\mathbf{C}}_c$ using the eigenvector corresponding to the largest eigenvalue of $\hat{\mathbf{C}}_c$.

V. Simulation results

As a simulation example, we consider a 3.6 mm diameter circular transducer with a coding mask, and a maximum mask thickness of 0.65 mm. As imaging region we choose all pixels on a Cartesian grid in a 3 by 3 mm square area in the (x,y) plane parallel to the transducer surface, at a depth of 6 mm. We assume that an initial estimate of $\mathbf{A}$ was obtained as described in Section II. The transducer transmit and receive transfer functions are slightly different, as shown in Fig. 1, where the true total impulse response $g_{tx}(t) * g_{rx}(t)$ is shown, as well as the estimated total impulse response $g_{tx}(t) * g_{tx}(t)$ as obtained by autoconvolution. The right panel in Fig. 1 also shows the ideal correction function $c(t)$ in the frequency domain: $c(\omega) = g_{rx}(\omega)/g_{tx}(\omega)$. The pulses are sampled at a sampling rate of 12 MHz. For simulations with a fixed calibration phantom, we generate an arbitrary $\mathbf{x}_c \sim \mathcal{N}(\mathbf{0}, \mathbf{I})$. For blind calibration simulations, we also generate each $\mathbf{x}_c$ from a Gaussian distribution: $\mathbf{x}_c \sim \mathcal{N}(\mathbf{0}, \mathbf{C}_x)$, and we use $\mathbf{C}_x = \mathbf{I}$.

First, we display some example reconstructions, with and without calibration. We set the measurement SNR

$$\text{SNR} = \text{trace}(\mathbf{A}\mathbf{A}^\mathsf{H})/(N\sigma_n^2) \tag{18}$$

to 20 dB for both the imaging experiment, as well as the calibration measurements. For the calibration with a known phantom, $\Phi = 50$ measurements were obtained by rotation, where a randomly generated $\mathbf{x}_c$ is fixed across all rotations. For the blind calibration technique, $K = 100$ measurements were

obtained, where each measurement is completely random and independent from other measurements (as described above). In Fig. 2, we show the true image compared to image reconstructions using a perfectly calibrated system, the incorrectly calibrated system, and the proposed calibration techniques. The R-shaped test phantom was adjusted to make it zero mean and unit variance. As can be seen, an un-calibrated model can cause a significant imaging error, and this is easily corrected by both calibration techniques.

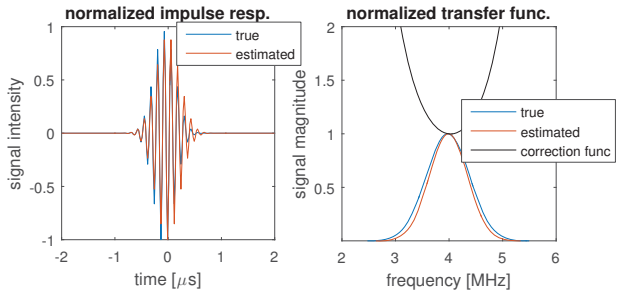

Fig. 1: Total electro-mechanical impulse responses: $g_{tx}(t) * g_{tx}(t)$ (initial estimate in $\hat{\mathbf{A}}$) and $g_{tx}(t) * g_{rx}(t)$ (true total impulse response) in the time domain (left), and the frequency domain (right). In the right panel we also display the DFT of the ideal solution $c(t)$.

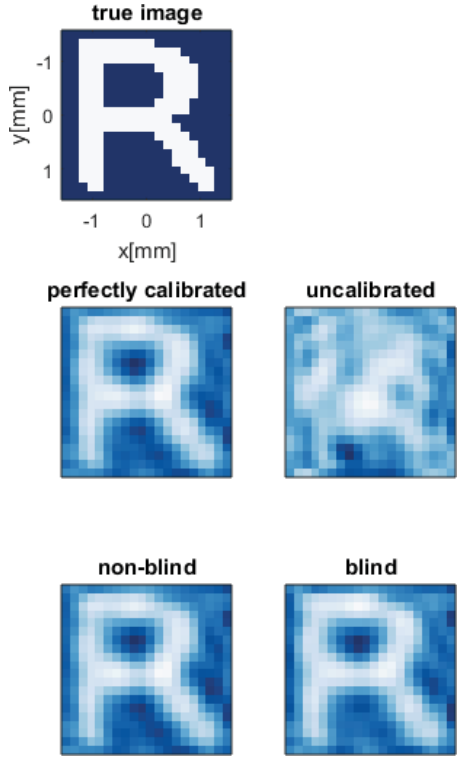

Fig. 2: Example reconstructions, compared to the true image (top), with a perfectly calibrated and uncalibrated model (middle rows), and using the proposed calibration techniques (bottom). Here, the calibration SNR is 20 dB, the imaging experiment SNR is 20 dB, and $\Phi = 50$, $K = 100$.

Finally, we perform a variety of calibration experiments for various SNR values. After calibration, we do an imaging experiment with the same R-shaped phantom, and compute the absolute normalized correlation between the estimated and true image as performance measure of the calibration technique. The SNR for the imaging experiments is fixed to 20 dB. For the blind calibration technique we consider a varying number of measurements ($K = 10, 50, 100$), and for the non-blind calibration technique we simulate for $\Phi = 10, 50$. In the case of non-blind calibration with a known phantom, we perform 100 calibration experiments per SNR, and compute the average absolute image reconstruction correlation using the calibrated model. Each phantom is generated with a different calibration random phantom (keeping the phantom fixed across all Φ measurements). For the blind calibration simulations, we perform 10 calibration experiments per SNR, and show the average absolute correlation.

The results are shown in Fig. 3. The perfectly calibrated model obtains a maximum correlation close to 0.9 (perfect correlation is difficult due to the ill-posedness of the inverse imaging problem). The calibration with a known phantom performs the best, which is expected since it is assumed the calibration phantom is known exactly, whereas the blind calibration algorithms have to account for the uncertainty of the calibration phantom.

When the SNR decreases, performance decreases for all techniques. The first calibration technique will try to 'fit' the estimate of $\mathbf{c}$ to the large measurement noise. For the second technique, the estimated measurement covariance matrix $\hat{\mathbf{C}}_y$ may not be accurate enough, and will be dominated by the error of the noise covariance matrix implicit in $\mathbf{C}_y$. If $\hat{\mathbf{C}}_y$ is not close enough to the true covariance $\mathbf{C}_y$, the blind calibration algorithm may not be able to find a low-rank solution to (14), and the resulting estimate of $\mathbf{c}$ will not necessarily be a good calibration signal. Consequently, the updated model may become less accurate, resulting in a decreased imaging performance.

VI. Conclusions and Discussion

We considered the problem of correcting an erroneously calibrated ultrasound pulse-echo model for a single sensor with a coding mask. Due to a mismatch between the transmit and receive impulse response of the single transducer, the used model may contain modeling errors causing a decrease of imaging quality. To obtain a better pulse-echo model, we proposed two calibration methods. One uses multiple measurements of the same, but known, calibration image, and the other uses many different random calibration images, knowing only the second order statistics of these images. We showed that, with sufficient SNR, both techniques are able to improve the pulse-echo model, resulting in better imaging performance. The blind calibration algorithm performs worse, especially for lower SNR, due to the uncertainty about the calibration image.

Our simulation results show that the models calibrated using low SNR measurements cause a deteriorated imaging quality, even compared to the uncalibrated model. Nevertheless, the

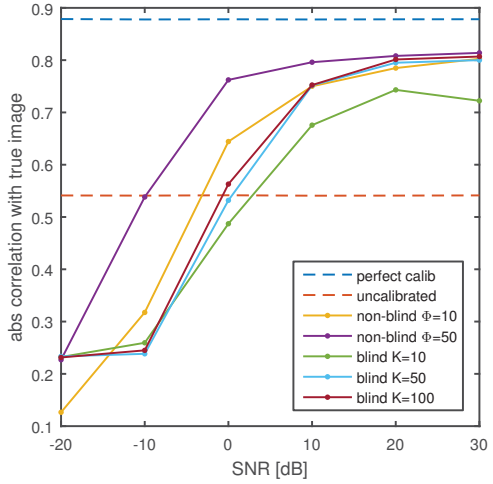

Fig. 3: Average absolute normalized correlation between the true test image and the estimated image using a (non)-calibrated pulse-echo model, for various SNRs.

correlations shown in Fig. 3 give an overly pessimistic view on the imaging performance. If one were to take into account the uncertainty in $\hat{\mathbf{A}}$, a better imaging performance could already be obtained by increasing the regularization parameter λ in (2), even though the measurement noise did not increase. Using a more optimal estimate, taking the modeling noise into account, will result in better performance for all calibration techniques in this paper.

REFERENCES

[1] J. A. Jensen, "Deconvolution of ultrasound images," *Ultrasonic imaging*, vol. 14, no. 1, pp. 1–15, 1992.

[2] R. Stoughton and S. Strait, "Source imaging with minimum mean-squared error," *The Journal of the Acoustical Society of America*, vol. 94, no. 2, pp. 827–834, 1993.

[3] J. Shen and E. S. Ebbini, "A new coded-excitation ultrasound imaging system. i. basic principles," *IEEE transactions on ultrasonics, ferroelectrics, and frequency control*, vol. 43, no. 1, pp. 131–140, 1996.

[4] R. Lavarello, F. Kamalabadi, and W. D. O'Brien, "A regularized inverse approach to ultrasonic pulse-echo imaging," *IEEE transactions on medical imaging*, vol. 25, no. 6, pp. 712–722, 2006.

[5] F. Viola and W. F. Walker, "Adaptive signal processing in medical ultrasound beamforming," in *Ultrasonics Symposium, 2005 IEEE*, vol. 4. IEEE, 2005, pp. 1980–1983.

[6] F. Viola, M. A. Ellis, and W. F. Walker, "Time-domain optimized near-field estimator for ultrasound imaging: Initial development and results," *IEEE Transactions on Medical Imaging*, vol. 27, no. 1, pp. 99–110, 2008.

[7] B. Byram, K. Dei, J. Tierney, and D. Dumont, "A model and regularization scheme for ultrasonic beamforming clutter reduction," *IEEE transactions on ultrasonics, ferroelectrics, and frequency control*, vol. 62, no. 11, pp. 1913–1927, 2015.

[8] B. Berthon, P. Morichau-Beauchant, J. Porée, A. Garofalakis, B. Tavitian, M. Tanter, and J. Provost, "Spatiotemporal matrix image formation for programmable ultrasound scanners," *Physics in Medicine & Biology*, vol. 63, no. 3, p. 03NT03, 2018.

[9] M. F. Schiffner and G. Schmitz, "Fast pulse-echo ultrasound imaging employing compressive sensing," in *Ultrasonics Symposium (IUS), 2011 IEEE International*. IEEE, 2011, pp. 688–691.

[10] N. Wagner, Y. C. Eldar, and Z. Friedman, "Compressed beamforming in ultrasound imaging," *IEEE Transactions on Signal Processing*, vol. 60, no. 9, pp. 4643–4657, 2012.

[11] C. Quinsac, A. Basarab, and D. Kouamé, "Frequency domain compressive sampling for ultrasound imaging," *Advances in Acoustics and Vibration*, vol. 2012, 2012.

[12] H. Liebgott, R. Prost, and D. Friboulet, "Pre-beamformed rf signal reconstruction in medical ultrasound using compressive sensing," *Ultrasonics*, vol. 53, no. 2, pp. 525–533, 2013.

[13] T. Chernyakova and Y. Eldar, "Fourier-domain beamforming: the path to compressed ultrasound imaging," *IEEE transactions on ultrasonics, ferroelectrics, and frequency control*, vol. 61, no. 8, pp. 1252–1267, 2014.

[14] G. David, J.-l. Robert, B. Zhang, and A. F. Laine, "Time domain compressive beam forming of ultrasound signals," *The Journal of the Acoustical Society of America*, vol. 137, no. 5, pp. 2773–2784, 2015.

[15] A. Besson, D. Perdios, F. Martinez, Z. Chen, R. E. Carrillo, M. Arditi, Y. Wiaux, and J.-P. Thiran, "Ultrafast ultrasound imaging as an inverse problem: Matrix-free sparse image reconstruction," *IEEE transactions on ultrasonics, ferroelectrics, and frequency control*, vol. 65, no. 3, pp. 339–355, 2018.

[16] D. L. Donoho, "Compressed sensing," *IEEE Transactions on information theory*, vol. 52, no. 4, pp. 1289–1306, 2006.

[17] E. J. Candès, J. Romberg, and T. Tao, "Robust uncertainty principles: Exact signal reconstruction from highly incomplete frequency information," *IEEE Transactions on information theory*, vol. 52, no. 2, pp. 489–509, 2006.

[18] E. J. Candes and T. Tao, "Near-optimal signal recovery from random projections: Universal encoding strategies?" *IEEE transactions on information theory*, vol. 52, no. 12, pp. 5406–5425, 2006.

[19] P. Kruizinga, P. van der Meulen, A. Fedjajevs, F. Mastik, G. Springeling, N. de Jong, J. G. Bosch, and G. Leus, "Compressive 3d ultrasound imaging using a single sensor," *Science advances*, vol. 3, no. 12, 2017.

[20] J. Janjic, P. Kruizinga, P. van der Meulen, G. Springeling, F. Mastik, G. Leus, J. G. Bosch, A. F. van der Steen, and G. van Soest, "Structured ultrasound microscopy," *Applied Physics Letters*, vol. 112, no. 25, p. 251901, 2018.

[21] T. L. Szabo, *Diagnostic ultrasound imaging: inside out*. Academic Press, 2004.

[22] E. K. Sittig, "Transmission parameters of thickness-driven piezoelectric transducers arranged in multilayer configurations," *IEEE transactions on Sonics and Ultrasonics*, vol. 14, no. 4, pp. 167–174, 1967.

[23] G. E. Tupholme, "Generation of acoustic pulses by baffled plane pistons," *Mathematika*, vol. 16, no. 2, pp. 209–224, 1969.

[24] P. R. Stepanishen, "The time-dependent force and radiation impedance on a piston in a rigid infinite planar baffle," *The Journal of the Acoustical Society of America*, vol. 49, no. 3B, pp. 841–849, 1971.

[25] J. A. Jensen, "A model for the propagation and scattering of ultrasound in tissue," *The Journal of the Acoustical Society of America*, vol. 89, no. 1, pp. 182–190, 1991.

[26] P. Dijkmans, L. Juffermans, R. Musters, A. van Wamel, F. Ten Cate, W. van Gilst, C. Visser, N. de Jong, and O. Kamp, "Microbubbles and ultrasound: from diagnosis to therapy," *European Journal of Echocardiography*, vol. 5, no. 4, pp. 245–246, 2004.

[27] A. Van Wamel, K. Kooiman, M. Harteveld, M. Emmer, J. Folkert, M. Versluis, and N. De Jong, "Vibrating microbubbles poking individual cells: drug transfer into cells via sonoporation," *Journal of controlled release*, vol. 112, no. 2, pp. 149–155, 2006.

[28] B. Ottersten, P. Stoica, and R. Roy, "Covariance matching estimation techniques for array signal processing applications," *Digital Signal Processing*, vol. 8, no. 3, pp. 185–210, 1998.

[29] S. J. Wijnholds and A.-J. Van Der Veen, "Multisource self-calibration for sensor arrays," *IEEE Transactions on Signal Processing*, vol. 57, no. 9, pp. 3512–3522, 2009.

[30] K. Nambur Ramamohan, S. P. Chepuri, D. F. Comesana, and G. Leus, "Blind calibration of sparse arrays for doa estimation with analog and one-bit measurements," in *ICASSP 2019*, to appear.